Evaluating Regional Changes in Temperature and Radiative Forcings over Germany in Observations and EURO-CORDEX Climate Model Simulations

Faculty of Physics and Astronomy
& MPI for Biogeochemistry

August 22, 2024

Bachelor Thesis

In fulfillment of the requirements for the degree
Bachelor of Science in Physics

Submitted by

Annegret Rößler

Supervisor: Prof. Dr. Gerhard Georg Paulus
Secondary Assessor: Dr. Axel Kleidon

With Maximum Power comes
Maximum Responsibility.

Uncle Ben, Earth System Thinker

Abstract

Climate model simulations at regional resolution are essential for understanding temperature trends. However, they seem to underestimate the observed warming in Germany. This work evaluates temperature responses to radiative forcings in two prominent Euro-CORDEX climate model simulations and their projections over Germany from 1961 to 2020. First, the climatological bias is analyzed by comparing 1961-1990 model data with DWD observations. A slight positive bias in air temperature in the simulations is noted, consistent with downwelling short- and longwave radiation in the surface energy balance. I use the period 1991-2020 with RCP 8.5 projections for change analysis. Temperature changes between the two periods seem to be underestimated by 20 to 40 % compared to observations. The surface energy balance is used to diagnose the contribution of short- and downwelling longwave radiation to these changes. Simulated downwelling longwave radiation shows a similar mean increase to observations but has a narrower and differently distributed spatial pattern of change. Simulated net shortwave radiation changes are less pronounced than observed or show an opposite trend, resulting in weaker warming or even a cooling temperature response. In contrast, observations show a substantial increase in net solar radiation, significantly contributing to the warming. To conclude, the models underestimate the observed warming in Germany due to missed increase in solar radiation.

Contents

1 Introduction

1.1 Motivation

Global warming is widely recognized as one of the key challenges of our time. It affects all areas of the atmosphere, oceans, cryosphere and biosphere, and every region in the world. (Intergovernmental Panel on Climate Change (IPCC), 2023) Over land, the warming is more pronounced than in the global average. Over Europe and Germany in particular, the observed and projected warming is even stronger than in the global average over land (Kaspar et al., 2023).

One way to describe this warming is by the surface energy balance of the earth, i.e. the radiative balance between absorbed and released heat at ground level. Incoming radiation is divided into solar and thermal radiation, also referred to as downwelling shortwave and longwave radiation. Outgoing radiation is thermal radiation emitted from the surface which we measure as temperature, and turbulent fluxes transporting energy through convection (National Oceanic and Atmospheric Administration, 2023). Solar radiation, specifically net solar radiation, is the radiation the surface of the Earth receives from the sun. Variations of it can dictate climate development over shorter and longer timescales (BUDYKO, 1969). Thermal radiation is the greenhouse effect, i.e. water vapor and other greenhouse gases in the atmosphere re-emitting thermal radiation back to the surface. Its variation is considered the key driver of anthropogenic climate change (IPCC Working Group I, 2021).

Climate models use fundamental laws of e.g. physics, chemistry and fluid dynamics to portray the climate system and its interactions. Climate model simulations aim to capture the historical development of the climate and to provide reliable projections of future trends, e.g. of temperature. Global climate models cover the whole planet and work on a coarse grid scale, making it difficult to distinguish regional trends. Regional climate models apply to specific areas and provide more details based on e.g. topography and land use. (IPCC Working Group I, 2021) In the "Coordinated Regional Climate Downscaling Experiment" CORDEX, regional climate projections were developed to amend global projections of the Coupled Model Intercomparison Project 5 (CMIP5) for the 5th assessment report of IPCC. The European branch of this project is coordinated by EURO-CORDEX. Additionally, the ReKliEs-DE project provided more detailed inview into these regional projections for Germany (DWD, 2018).

These model simulations and projections are an integral part of climate mitigation and adaptation decision-making. They are essential for the German climate outlook and its regional divisions (Pfeifer et al., 2020).

1.2 Objective

This analysis will evaluate temperature changes over the years 1961-2020 based on radiative forcings' impact on the surface energy balance over Germany in observations and regionalized climate model simulations from the European Domain of the Coordinated Downscaling Experiment (EURO-CORDEX). It will take into account the climatological bias in the period 1961-1990 in the simulations.

1.3 Hypotheses

In this work, I will examine two hypotheses emerging from this approach:

1. The temperature analysis via the surface energy balance over Germany in climatological timescales at a regional grid scale is possible and adequate.

2. The radiative forcing through an increase of net solar radiation is significantly underestimated in climate model simulations, leading to underestimated temperature responses and hence an underestimation of the already observed temperature increase over Germany between 1961 and 2020.

2 Fundamentals

This section provides definitions of used terms and the physical background of the key concept of this work, the surface energy balance. Further, climate models and the EURO-CORDEX project are briefly explained.

2.1 Climate and climate change

Climate describes the average weather conditions, e.g. temperature, precipitation and wind over a long period. The classical climatological period covering 30 years (World Meteorological Organization, 2024). *Climate change* describes change over several climatological periods. (Benestad et al., 2021) In this analysis, the examined periods are 1961-1990, which I will refer to as the *reference period*, and 1990-2020, which I will refer to as the *change period*. This work refers to the bias of the examined variables over the reference period as *climatological bias* and to the bias of differences between the change period and the reference period as *change bias*.

2.2 Surface energy balance of the Earth

The *surface energy balance* of the earth describes the equilibrium of incoming and outgoing radiation at the Earth's surface and dictates the variables to be examined in this work (National Oceanic and Atmospheric Administration, 2023).

Unless indicated otherwise, the following definitions are based on the glossary of the physical science basis of IPCC's 6th synthesis report (IPCC Working Group I, 2021).

Incoming Radiation is net solar radiation and downwelling longwave radiation.

Net solar radiation describes absorbed solar radiation that remains after solar radiation arriving at the top of the atmosphere is scattered by clouds and aerosols in the Earth's atmosphere and reflected at its surface. Incoming solar radiation is often referred to as downwelling shortwave radiation or global radiation Net solar radiation is determined by downwelling and upwelling solar radiation, the latter describes partition of downwelling solar radiation that is reflected at the surface. It is usually expressed through *albedo* as the ratio between upwelling to downwelling shortwave radiation.

Downwelling longwave radiation describes the greenhouse effect, i.e. the thermal radiation arriving at the surface from the atmosphere emitted by water vapor and other greenhouse gases. This is why it it often referred to as downwelling thermal radiation.

Outgoing Radiation is emitted thermal radiation of the Earth and turbulent fluxes (IPCC Working Group I, 2021).

The emitted thermal radiation of the earth describes the black body radiation of the Earth that ultimately quantifies the *surface temperature*.

The term *turbulent fluxes* includes surface latent heat flux and surface sensible heat flux. Both describe energy output that is not expressed by temperature. Surface latent heat flux describes energy transfer associated with evaporation. Surface sensible heat flux describes energy transfer due to temperature differences between the surface and the air.

This analysis focuses on *radiative forcings*. By that, I mean change in incoming radiation entailing an impact on the whole energy balance, forcing the outgoing radiation to change to keep the equilibrium. The forcing is given in watts per square meter, i.e. the radiative flux change.

The term *climate sensitivity* is commonly used to refer to temperature responses to rising CO_2 concentrations that are expressed through rise in downwelling longwave radiation. However, it is not constrained to only that and can be used to describe temperature responses to change in different radiative fluxes, such as solar radiation (Klima, 2023).

The surface energy balance of the earth can be hence described by the following equation:

$$R_s + R_{ld} = \sigma T_s^4 + J \tag{2.1}$$

with

$$R_s = R_{sd} \cdot (1 - \alpha), \tag{2.2}$$

where R_s is net shortwave radiation in watts per square meter (W/m^2), R_{ld} is downwelling longwave radiation in W/m^2, σT_s^4 is the blackbody radiation on the Earth, where σ the Stefan-Boltzmann constant ($\sigma = 5.67 \cdot 10^{-8}$ $W/(m^2 \cdot K)$ and T_s is the surface temperature in Kelvin (K) and J is the ensemble of turbulent fluxes in W/m^2. R_{sd} is downwelling solar radiation in W/m^2 and α is albedo (no units or %).

Thus, the surface energy balance is solely based on radiation at the Earth's surface from the atmospheric column and neglects other meteorological components, such as wind, and further interactions in or above the ground.

To express small changes in the energy balance, it is linearized, leading to:

$$\Delta R_s + \Delta R_{ld} = 4 \cdot \sigma \cdot T_i^3 \cdot \Delta T + \Delta J. \tag{2.3}$$

This leads to the following two equations to diagnose surface temperature T_s and surface temperature change ΔT_s

$$T_s = \left[\frac{R_s + R_{ld} - J}{\sigma} \right]^{\frac{1}{4}} \tag{2.4a}$$

$$\Delta T_s = \frac{\Delta R_s + \Delta R_{ld} - \Delta J}{4 \cdot \sigma \cdot T_i^3}. \tag{2.4b}$$

The linearization term is preferred over computing the absolute temperature for both examined periods and simply taking the difference because it takes into account the initial temperature conditions which have an impact on climate sensitivity.

2.3 Climate Model Simulations, Projections and RCPs

The descriptions in this section are based on the glossary of the physical science basis of IPCC's 6th synthesis report (IPCC Working Group I, 2021) and the Guidance for EURO-CORDEX climate projections data use (Benestad et al., 2021).

A *climate model* represents the climate system qualitatively or quantitatively based on physical, chemical and biological properties, interactions and feedbacks of its constituents. They aim to give an insight into monthly, seasonal or interannual past and future climate change. They vary in complexity and regionality. A *climate model simulation* is a numerical simulation taking into account climate interactions and feedbacks based on different baseline assumptions.

A *climate projection* is a simulated future response to changes in climate forcings based on climate models. These forcings usually include anthropogenic impact such as future emissions of greenhouse gases leading to enhanced concentrations of them, and aerosol or land use changes. They are distinguished from climate predictions by their dependence on the used forcing scenario.

One way to distinguish scenarios are *Representative Concentration Pathways* (RCPs). They include projected temporal development of the formerly listed anthropogenic forcings. They are called *representative* because they provide one of many possible scenarios with specific radiative forcings. They are called *pathways* to emphasize the temporal development, not only the resulting concentration of e.g. greenhouse gases. The pathways are named by the assumed radiative forcing by the year 2100. There are three common RCPs in use: *RCP2.6* where radiative forcing peaks at $3\,W/m^2$ and is reduced to $2.6\,W/m^2$ by 2100, an intermediate *RCP4.5* assuming stabilized radiative forcing of $4.5\,W/m^2$ by 2100 and *RCP8.5* that assumes higher emissions leading to a radiative forcing of above $8.5\,W/m^2$ by the end of the century.

2.4   EURO-CORDEX

EURO-CORDEX is the European branch of the CORDEX (coordinated downscaling experiment) initiative that was created by the Task Force for Regional Climate Downscaling (TFRCD) by the World Climate Research Programme (WCRP) in 2009, with the goal to generate regional climate change projections all over the world. This was within the time of the Fifth Assessment Report of IPCC (around 2014). EURO-CORDEX produced 55 ensemble climate simulations, consisting of downscaling or regional climate models (RCM) forced by global climate models from the Coupled Model Intercomparison Project Phase 5 (CMIP5) ((Benestad et al., 2021) and (DWD, 2018)). In combining a global (GCM) and a regional climate model (RCM), the regional climate model is used for downscaling a global climate model but keeps the simulated overall climate of the global model (Hübener; Spekat, et al., 2018).

The simulations and projections include historical data from 1950 to 2005 and projected data from 2006 to 2100. The smallest grid scale to which the simulation are regionalized is $0.11\,° \times 0.11\,°$ (approx. $12.5\,km \times 12.5\,km$).

A selection of variables in a selection of global and regional climate models from the EURO-CORDEX ensemble have been evaluated in the ReKliEs-DE project (Hübener; Bülow, et al., 2018) which will be referred to in certain points in this analysis. ReKliEs-DE mostly focuses on projections and uses a different reference period than this analysis so the references I will use are merely qualitative.

3 Methods

3.1 Evaluation Plan

The evaluation will use three main steps: First, I analyze the climatological bias of the simulations in the reference period which consists of the years 1961 to 1990. Second, I analyze the bias in the already observed change between the 1991 to 2020 and the reference period. Third, I will attribute the temperature change to different radiative forcings.

3.2 Maximum power limit of the atmosphere

The Maximum Power approach offers a way to deal with turbulent fluxes in the energy balance. It implies that they work equivalent to a "cold" heat engine and near the Carnot limit of said heat engine. This approach accounts for how much convection is thermodynamically possible based on local radiative forcing. It leads to the following optimum heat flux in the absence of heat storage changes in the lower atmosphere (Kleidon; Renner, 2018)

$$J = \frac{R_s}{2} \,. \tag{3.1}$$

This estimates the unknown turbulent upward fluxes and will be used for this analysis.

When including this approach in the radiation term of the surface energy balance $R_s + R_{ld} - J$, the resulting equation for surface temperature and surface temperature change depends solely on net solar and downwelling longwave radiation

$$T_s = \left[\frac{R_s/2 + R_{ld}}{\sigma} \right]^{\frac{1}{4}} \tag{3.2}$$

and

$$\Delta T_s = \frac{\Delta R_s/2 + \Delta R_{ld}}{4 \cdot \sigma \cdot T_i^3} \,. \tag{3.3}$$

To diagnose the impact of each radiative forcing, the term for ΔT_s can be split up into the following terms

$$(\Delta T_s)_{\text{solar}} = \frac{\Delta R_s}{2} \cdot (4 \cdot \sigma \cdot T_i^3)^{-1} \,, \tag{3.4a}$$

$$(\Delta T_s)_{\text{ld}} = \Delta R_{ld} \cdot (4 \cdot \sigma \cdot T_i^3)^{-1} \,. \tag{3.4b}$$

Hence, with the same initial conditions, the temperature response to R_s forcing is half as big as the response to R_{ld} forcing. Generally, due to climate sensitivity, the temperature response to both kinds of radiation depends strongly on initial temperature.

Given the turbulent fluxes operate at maximum power, knowledge of three variables is necessary for the evaluation: Temperature for a general overview of the temperature and its development, and net solar and downwelling longwave radiation to diagnose radiative forcings and their temperature response.

3.3 The Datasets

Firstly, a temperature term is needed to enable this evaluation for temperature bias analysis and as reference for the surface temperature. This work will use air temperature close to the surface at 2m height. An additional step in the analysis is performed to validate the use of air temperature instead of surface temperature at climatological timescales. Secondly, knowledge about the radiative fluxes is necessary to describe radiative forcings and the surface energy balance. With Maximum Power, the variables are reduced to only two radiative terms: net solar radiation R_s and downwelling longwave radiation R_{ld}.

Observations will be covered by DWD-HYRAS. As simulation data, I chose two prominent simulations from the EURO-CORDEX project.

3.3.1 The observations – DWD-HYRAS

HYRAS, short for *Hydrometeorological Raster Dataset*, is a dataset of various hydrometeorological variables for Germany and the neighboring river basins. It is provided by Deutscher Wetterdienst and will further be referred to as DWD-HYRAS or observations. It includes 2 m air temperature (minimum, maximum and mean), precipitation, downwelling solar radiation (called radiation global in the dataset) and relative humidity. All variables are given as daily means in a 5 km x 5 km grid. It is a station-based dataset, i.e. the data consists of mesasurements from weather stations, interpolated and partly suported by reanalysis data to provide continuous data over the whole grid (DWD, 2020d).

Temperature
DWD-HYRAS provides air temperature at 2 m height (DWD, 2020c).

Net Solar Radiation and Albedo
Downwelling solar radiation is provided in the HYRAS dataset under the name "radiation global". (DWD, 2020a). Upwelling shortwave radiation to quantify albedo is not provided, so a constant albedo of 15 % is assumed over the whole grid, hence

$$\alpha_{\text{HYRAS}} = 15\% = \text{const.} \tag{3.5}$$

Downwelling longwave radiation
Downwelling longwave radiation is not part of the HYRAS dataset. However, it can be diagnosed via the Brutsaert (Brutsaert, 1975) equation through air temperature and humidity (DWD, 2020b)

$$R_{\text{ld, cs}} = \varepsilon_{\text{cs}} \cdot \sigma \cdot T_{\text{air}}^4. \tag{3.6}$$

Where $R_{\text{ld, cs}}$ is downwelling longwave radiation for clear sky conditions, ε_{cs} is the clear-sky emissivity of the atmosphere, σ is the Stefan-Boltzmann-constant and T_{air} is air temperature. Clear sky conditions imply that cloud cover is neglected.

The clear-sky emissivity is calculated via

$$\varepsilon_{\text{cs}} = 1.24 \left(\frac{e_a}{T_{\text{air}}} \right)^{\frac{1}{7}}, \tag{3.7}$$

where e_a is the 2 m water vapor pressure, depending on relative humidity *RH* through (Cai, 2019)

$$e_a = \frac{RH}{100} \cdot e_s, \tag{3.8}$$

where e_s is saturation water vapor pressure that can be estimated through relative humidity and (dewpoint) temperature (Tian et al., 2023).

Deriving Rld through Brutsaert was not part of this analysis, $R_{ld, Brutsaert}$ was a dataset provided by my supervisor Dr Axel Kleidon.

Through the clear-sky conditions in Brutsaert, a positive bias is noted in $R_{ld, B}$ that will be estimated and corrected through CERES satellite data (NASA-CERES, 2024 Kato et al., 2018) for downwelling longwave radiation that is available for the years 2001-2020. Details including a map of $R_{ld, Brutsaert}$ for the period 2001-2020 can be found in the Appendix (A.5).

This correction ultimately leads to

$$R_{ld} = R_{ld, Brutsaert} \cdot 0.95 \tag{3.9}$$

for downwelling longwave radiation in the observations. This includes the magnitude correction from CERES satellite observations but retains the spatial distribution provided by the humidity measurements at regional scale.

3.3.2 EURO-CORDEX climate model simulations

Out of the 55 EURO-CORDEX simulations, two prominent combinations of driving global climate models (GCM) and regional climate models (RCM) were chosen for this analysis.

The first driving global climate model is HadGEM2-ES provided by the UK Met Office Hadley Centre. The picked regional climate model is GERICS-REMO2015, provided by the Max-Planck-Institute for Meteorology, Hamburg, including climate projections by Climate Service Center GERICS. It will be abbreviated as HadGEM2/REMO2015 in the text.

The second driving global climate model is MPI-M-ESM-LR provided by the Max-Planck-Institute for Meteorology. The picked regional climate model is MPI-CSC-REMO2009

It will be abbreviated as MPI-LR/REMO2009 in the text.

According to the results report of the Rekliesde project, simulations driven by the GCM HadGEM2 are at the upper part of the temperature range of all simulations and the MPI-LR-driven simulations are in the middle of the range. Regarding temperature trends, a HadGEM-driven model portrays among the strongest trends and an MPI-LR-driven model among the weakest trends (Hübener; Bülow, et al., 2018). Thus, I expect to get an inview into the magnitude and range of the model bias in climatology and change.

All variables were accessed as monthly means at a grid scale of $0.11° \times 0.11°$ (approx. $12.5\,\mathrm{km} \times 12.5\,\mathrm{km}$) via Copernicus Climate Change Service (Copernicus Climate Change Service, 2019) for the years 1961-2020 in 10-year-bundles.

Temperature

The simulations provide air temperature at 2 m height.

Net solar radiation and albedo

In addition to downwelling shortwave radiation, the upwelling shortwave radiation is also provided, i.e. here, net solar radiation R_S at the surface is diagnosed by subtracting the latter from the former. Thus, one regionally dependent albedo value results for each gridpoint

$$\alpha_{\text{Simulations}} = \frac{R_{\text{su}}}{R_{\text{sd}}} . \tag{3.10}$$

A visualization of albedo distribution over the reference period and change in the simulations can be found in the Appendix (A.4).

Downwelling longwave radiation

In the simulations, downwelling longwave radiation R_{ld} is provided as a variable and does not need to be further adjusted.

Data analysis and visualization

The tools used for the data analysis are climate data operators (cdo) for initial analysis steps, with great support from the cdo users guide (Schulzweida, 2016) and Python for further computing and visualization.

To enable comparison at gridscale, all datasets have to be in the same grid. Here, I choose the 12 km grid of the two simulations and regrid the DWD-HYRAS data from its finer 5 km grid to the coarser grid of Euro-CORDEX.

The following steps were performed via CDO. They mostly served the purpose of reducing further computation time:

- Merging the 10-year datasets to one big dataset per variable
- Cropping the datasets spatially to a box around Germany
- Regridding DWD-HYRAS data to the CORDEX grid
- Averaging DWD-HYRAS data from daily means to monthly and yearly means.

Then, the datasets were opened in python for further analysis steps:

- Masking the data to fit the Germany map
- Computing means and standard deviations
- Calculating surface temperatures and radiative forcings
- Visualizing the data in maps and scatter plots.

The following packages were used:

- NumPy for general array operations
- SciPy for linear regressions
- Matplotlib for visualization
- Cartopy to add geographic features and projections to the maps.

4 Results

This section is structured as follows: First, I analyze the climatological bias of the simulations in air temperature, net solar radiation and downwelling longwave radiation for the reference period 1961-1990. This leads to the reconstruction of temperature through radiative fluxes. Then, I will use these findings to analyze the changes between the reference period and the second period 1991-2020. This leads to an interpretation of temperature responses due to radiative changes. A detailed overview of mean values averaged over Germany and their standard deviation for every variable can be found in the Appendix (tables A.5 and A.6 in section A.3).

4.1 Climatological Bias in Reference Period

I will start this section off by analyzing the climatological bias in the reference period (1961-1990). The 30-year mean over this period in both simulations and observations for the variables air temperature T_{air}, net solar radiation R_{s} and downwelling longwave R_{ld} are portrayed in figure 4.1.

Air temperature shows similar properties throughout all three datasets. Figure 4.1a shows the mean air temperature T_{air} distribution. One can see topographic differences well aligning between the observations and simulations with mountainous regions recognizable through lower mean temperatures. Averaged over Germany, the simulations show a slight positive bias of $0.56\,\text{K}$ (HadGEM2/REMO2015) and $0.40\,\text{K}$ (MPI-LR/REMO2009), Thus, both the mean temperature and deviations through variation in topography appear to be well captured by the simulations.

In net solar radiation, one simulation shows a positive bias in the spatial mean. Figure 4.1b shows the net solar radiation R_{s} distribution. While both simulations show stronger spatial differences than the observations, the geographic patterns are similar. In southern regions, the radiative flux is higher than in the north while the weakest flux is noticed in the north-west with an increase toward eastern Germany. On the spatial mean, the two simulations diverge. MPI-LR/REMO2009 shows a slight negative bias of less than $-1\,W/m^2$ compared to observations, whereas HadGEM2/REMO2015 shows a mean positive bias of approximately $+7\,W/m^2$. The visible differences in spatial variability might partly, but not fully, be due to different assumptions on albedo as described in chapters 3.3.1, 3.3.2 and A.4.

The bias of the simulations in downwelling longwave radiation R_{ld} is smaller than in net solar radiation. In figure 4.1c, R_{ld} is portrayed. All three datasets show a similar spatial pattern with mountainous regions in the south emerging with weaker radiative flux. This aligns with the atmospheric column being smaller over elevated regions as opposed to lower regions, providing fewer particles to participate in emitting thermal radiation. Averaged over Germany, HadGEM/REMO2015 shows a negative bias of almost $-2\,W/m^2$, MPI-LR/REMO2009 one of less than $+1\,W/m^2$.

With the two incoming radiation terms and maximum power determining the outgoing radiative flux, surface temperature T_{surface} can now be computed using the surface energy balance, see equation (2.1). The results are presented in figure 4.2 in a scatterplot assigning the diagnosed surface temperature to given air temperature, both in Kelvin, for each grid point.
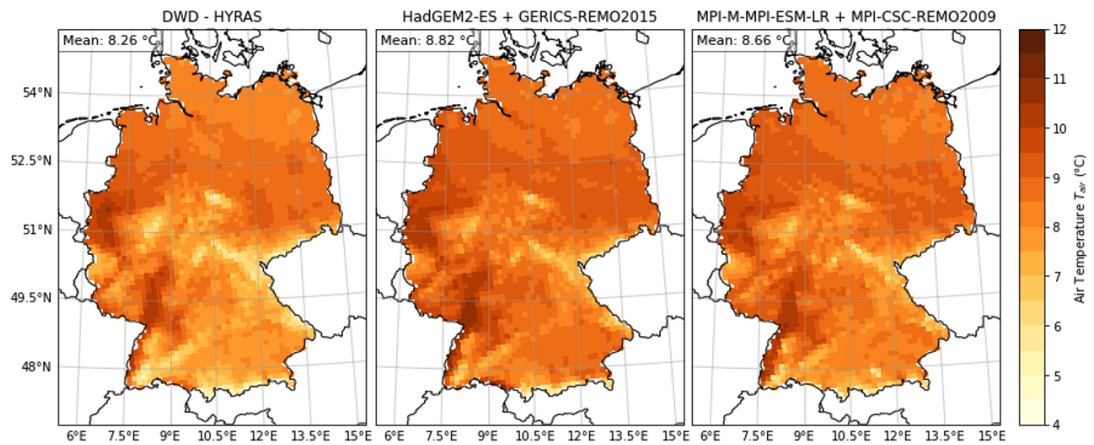
(a) Air temperature T_{air}.
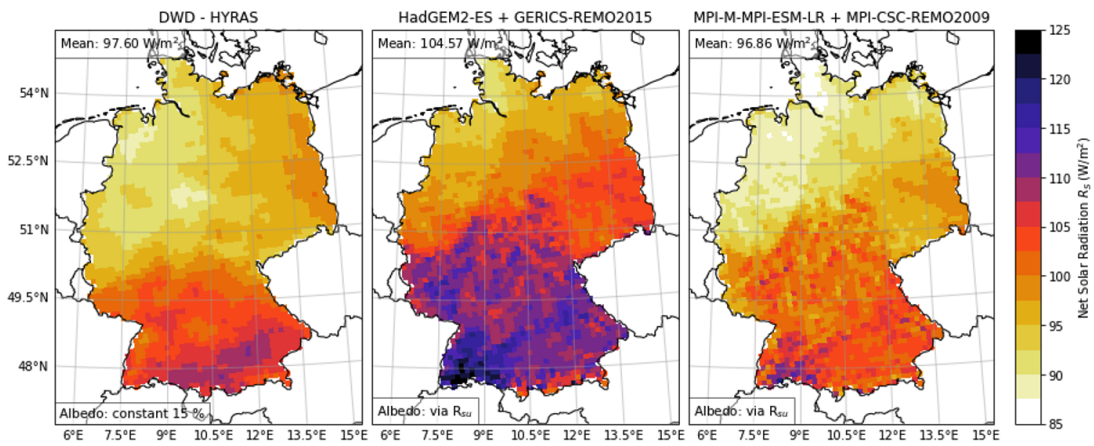
(b) Net solar radiation R_s, albedo included.
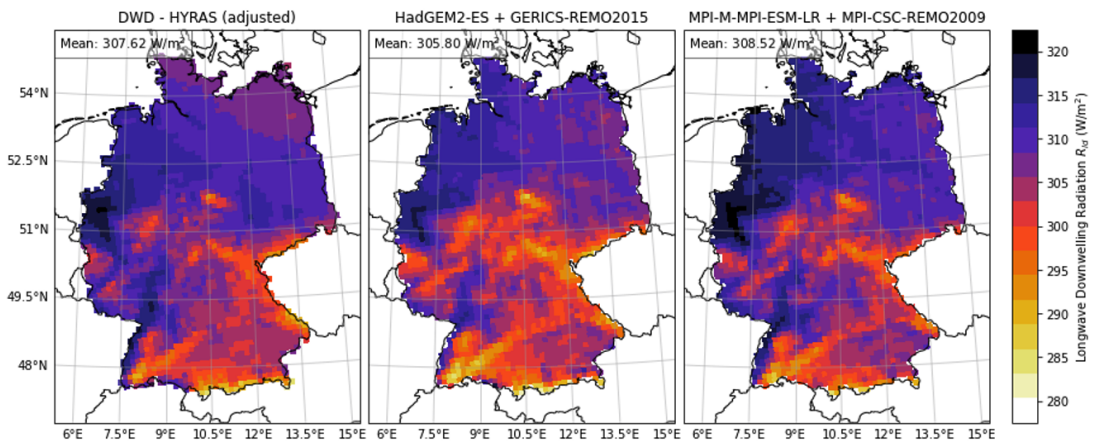
(c) downwelling longwave radiation R_{ld}.

Figure 4.1: Air temperature (top row (a)), net solar radiation (middle row (b)) and downwelling longwave radiation (bottom row (c)) in Germany averaged over the reference period 1961-1990 in observations from DWD-HYRAS (left) and simulations HadGEM2/REMO2015 (middle) and MPI-LR/REMO2009 (right). Spatial mean over Germany included (top left corner of each map).
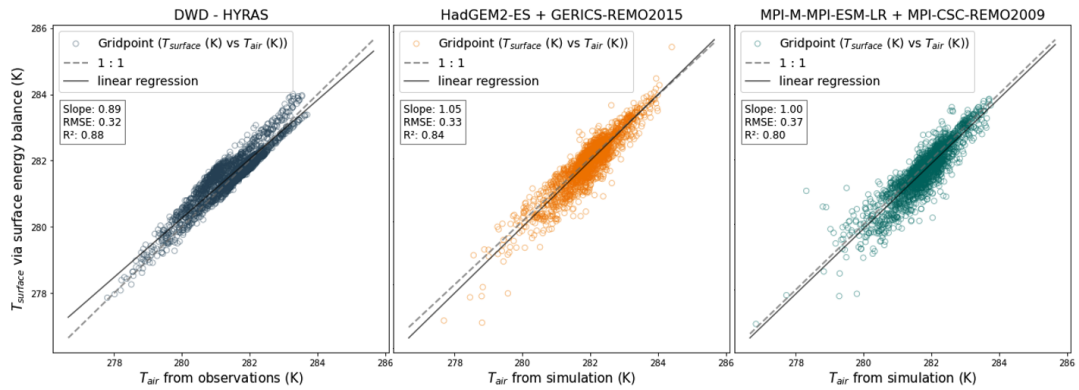
Figure 4.2: Mean surface temperature diagnosed via surface energy balance plotted against air temperature from the observations (left) and simulations HadGEM2/REMO2015 (middle) and MPI-LR/REMO2009 (right) for each gridpoint averaged over reference period 1961-1990. Linear regression line (black solid line) with properties (Slope, RMSE and R^2) and perfect correspondence (1:1) line (grey dashed line) included in each plot.

The diagnosed surface temperature corresponds very well to the provided air temperature in the reference period. The linear fit portrays a slope of 0.89 for observations with little scattering and an anticipated bifurcation towards he higher end of the temperatures. The slope is even closer to perfect correspondence in the simulations at 1.05 for HadGEM2/REMO2015 and 1.00 for MPI-LR/REMO2009 with a small offset. The root mean squared error (RMSE) values all within 0.33 and 0.37 emphasize the correspondence. Hence, over the whole grid, the diagnosed surface temperature aligns well with the given air temperature. The mean correspondence supports this finding. For DWD-HYRAS, the mean of the correspondence $T_{surface}/T_{air}$ is (1.000 ± 0.001). In the simulations, the values for $T_{surface}$ are slightly more scattered around the line for perfect correspondence, but this scattering does not affect the correspondence in significant ways, leading to the same mean correspondence values for HadGEM2/REMO2015 and MPI-LR/REMO2009. Scatterplots illustrating the bias of T_{air}, R_{s} and R_{ld} can be found in the Appendix (A.6).

This section confirms that the approach to assigning surface temperature to the radiative balance over the vertical atmospheric column via the surface energy balance with maximum power is adequate. Accordingly, at climatological timescales and regional grid scales, mean temperatures can be reconstructed via the surface energy balance. This enables the interchangeable use of $T_{surface}$ and T_{air} in this analysis and to interpret changes in temperature due to those of radiative fluxes.

4.2 Temperature and Radiation Change

I will go on to analyze air temperature change and temperature responses to changes in radiative fluxes between the change period 1991-2020 and the reference period 1961-1990. In the second period, the RCP projections start in 2005, i.e. the second half of this period contains two different pathways. Due to the limited number of years including different RCPs and making the resulting changes similar to one another, this part of the analysis is restricted to RCP 8.5. The corresponding plots for RCP 2.6 can be found in the Appendix (A.7).

Regarding air temperature change $\Delta(T_{air})$, the simulations deviate from the observations in spatial
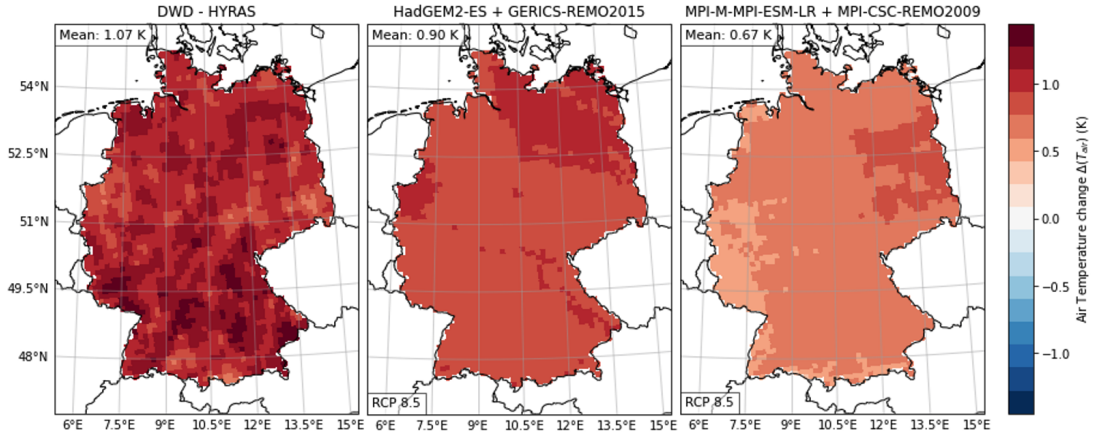
Figure 4.3: Air Temperature difference between period 2 (1991-2020) and period 1 (1961-1990) in observations (left) and simulations (HadGEM2/REMO2015 (middle) and MPI-LR/REMO2009 (right)) with RCP 8.5 projections, spatial mean over Germany included (top left corner of each map).

resolution and magnitude. $\Delta(T_{\text{air}})$ is presented in figure 4.3 for all three datasets over Germany. In the observations, distinctive regional differences can be seen with stronger heating spots in the south. Towards the north, $\Delta(T_{\text{air}})$ is slightly less pronounced with the area around Berlin presenting slightly more heating than its surroundings. In both simulations, the warming is rather uniform with a slight negative gradient from northeast to southwest in MPI-LR/REMO2009. The spatial average shows a negative bias in both simulations, whereas the warming is underestimated by around $0.2\,K$ in HadGEM2/REMO2015 and by $0.4\,K$ in MPI-LR/REMO2009. A scatterplot further visualizing this bias can be found in the Appendix (A.7, figure A.5).

In figure 4.4, the net solar radiation change ΔR_{s} and downwelling longwave radiation change ΔR_{ld} are plotted over the observed change in a scatterplot. Each colour represents one simulation with different marker shapes for each radiative flux change and each marker represents one gridpoint. Generally, one can see two key differences between the simulated and the observed change. The scattering of radiation change for both fluxes is significantly more narrow than shows in the observations. The magnitude of change in R_{s} has a strong downward deviation from the observations.

In downwelling longwave radiation change ΔR_{ld}, the values for both simulations lie within the same magnitude, i.e. between $+3.5\,W/m^2$ and $+5.5\,W/m^2$ where one can see that the change distribution is slightly narrower in HadGEM/REMO2015. In the observations, the change is distributed between $+1\,W/m^2$ and $+6.5\,W/m^2$ which speaks for stronger regional differences that seem not to be captured by either simulation. The magnitude of change in R_{ld} is similar to the observations with a slight positive bias, where the spatial mean is at $+4.21\,W/m^2$ in the observations, $+4.61\,W/m^2$ for HadGEM2/REMO2015 and $+4.47\,W/m^2$ for MPI-LR/REMO2009.
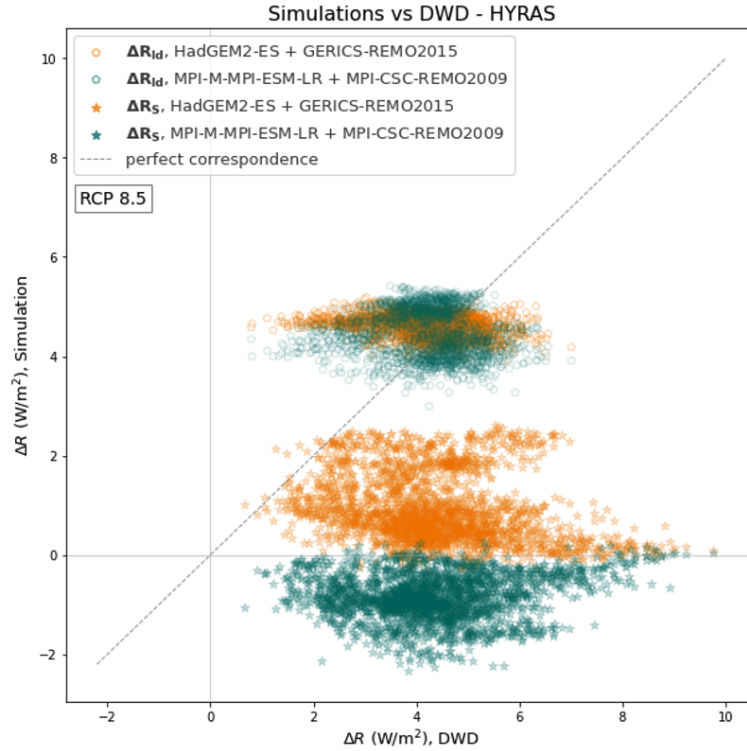
Figure 4.4: Mean net solar (solid stars) and downwelling longwave radiation (pentagons) change between period 2 (1991-2020) and period 1 (1961-1990) from simulations (HadGEM2/REMO2015 (orange) and MPI-LR/REMO2009 (green)) for RCP8.5 plotted against observed trends for each gridpoint, perfect correspondence line (grey dashed line) included.

Regarding net solar radiation change ΔR_s, the simulations deviate significantly from the observations and from each other. Both simulations portray much more uniform change covering a range of approx. $2 \, W/m^2$ where the observations show a range of approx. $7 \, W/m^2$. Regarding magnitude, both simulations show a strong negative bias. In DWD-HYRAS, R_s increases by $4.33 \, W/m^2$ from the first to the second period averaged over Germany. This change is significantly underestimated by both climate model simulations with an offset of $-3.40 \, W/m^2$ (HadGEM2/REMO2015) and $-5.17 \, W/m^2$ (MPI-LR/REMO2009). Hence, one simulation shows a slight increase where a strong increase is expected and the other portrays a decrease, not capturing any increase between the two periods.

4.3 Temperature Response to Radiative Forcings

The surface temperature response to the formerly described radiative forcings can now be diagnosed via the linearization of the surface energy balance. The spatial distribution of the results according to equations (3.4) with the terms for net solar and downwelling longwave radiation from equations (2.2), (3.5), (3.10) and (3.9) are shown in figure 4.5.

The temperature response to ΔR_s is portrayed in figure 4.5a. In DWD-HYRAS, clear regional trends can be identified with a stronger impact over parts of eastern Germany (Saxony, Saxony-Anhalt, Thuringia) and in some western regions close to the border. Smaller impact is noticeable in the north-east and south-east. As expected from previously analysed figure 4.4, this trend is not reflected in

14

the simulations. Not only can no significant regional differences be distinguished, but also is the temperature change by radiative change over the whole of Germany almost disappearing. While in HadGEM/REMO2015, the forcing by R_s is underestimated, it changes sign in MPI/REMO2009 and leads to cooling.
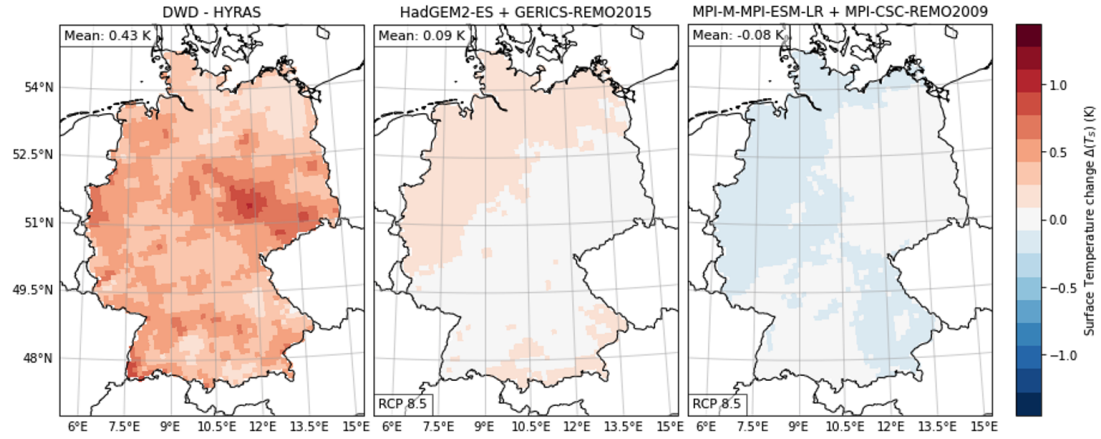
(a) Surface temperature response to net solar radiation change.
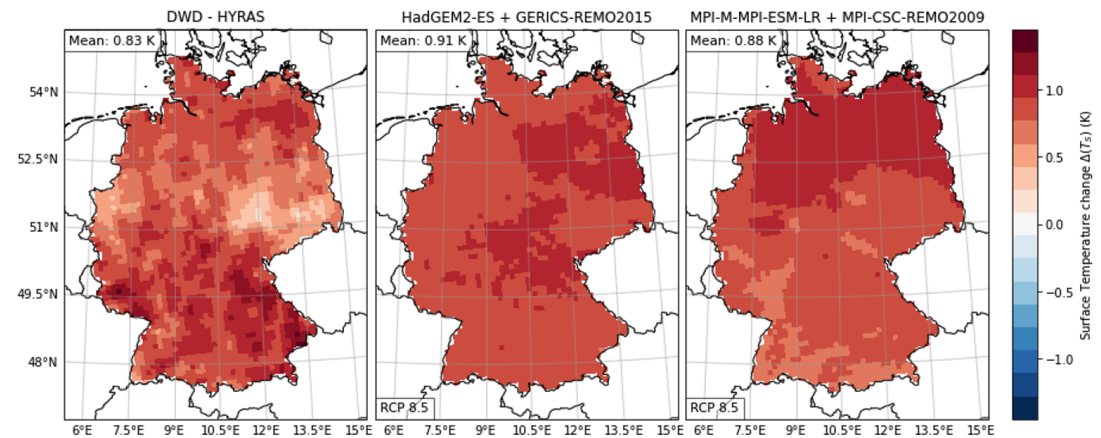
(b) Surface temperature response to downwelling longwave radiation change.

Figure 4.5: Surface temperature response to radiative forcings by net solar radiation (top row) and downwelling longwave radiation (bottom row) change in DWD-HYRAS observations (left) and HadGEM2/REMO2015 (middle) and MPI-LR/REMO2009 (right) climate model simulations for RCP 8.5 from the reference period 1961-1990 to the change period 1990-2020 over Germany. Spatial mean (upper left corner of graph) and scenario included (bottom left corner).

The temperature response to ΔR_{ld} is shown in figure 4.5b. Once again, the regional differences in DWD-HYRAS are clearly visible. The strongest effects can be noticed in the south, especially the south-east, like Bavaria, and towards the west, like Saarland. Weaker effects present themselves in almost the same areas where ΔR_s forcing apppears stronger. In the simulations, only a slight regional variation can be noticed in MPI-LR/REMO2009, where the response to R_{ld} forcing is decreasing towards the south as opposed to the observations where it is increasing from north to south. In terms of magnitude , all three datasets have a similar spatial mean but the simulations show a slight positive bias of $+0.08\,K$ (HadGEM/REMO) and $+0.05\,K$ (MPI/REMO2009).
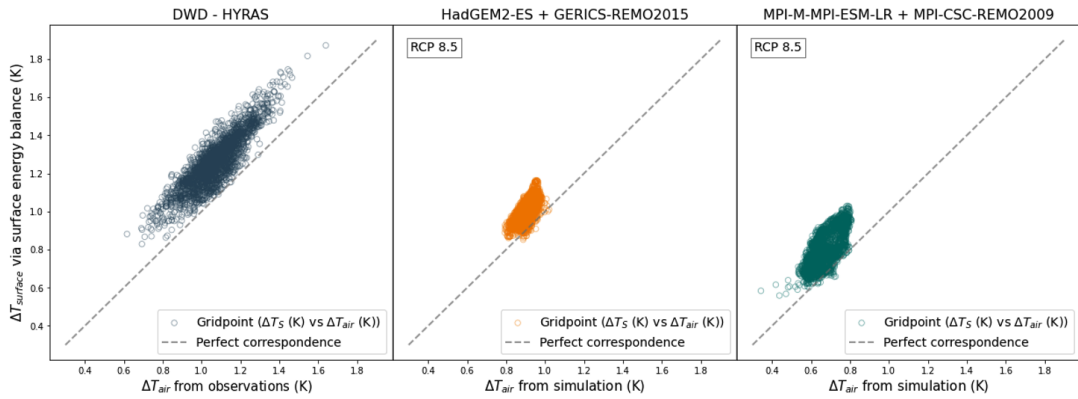
Figure 4.6: Mean surface temperature change diagnosed via surface energy balance plotted against air temperature change from the simulations and observations for each gridpoint between 1961-1990 and 1991-2020, perfect correspondence line (grey dashed line) included.

In figure 4.6, the computed $\Delta T_{\text{surface}}$ as a sum of the response to both radiative forcings is plotted over ΔT_{air} for observations and simulations. This visualizes once more the smaller spatial distribution of change in the simulations but also a positive bias in T_{surface}. This deviation might be due to the linearization of the surface energy balance. Normally, the initial temperature T_{i} would change over time, affecting the climate sensitivity to radiation increase while I used a fixed T_{i} and then worked with the mean over the analyzed periods, accumulating a certain bias in climate sensitivity i.e. the temperature response over these periods. Thus, for this analysis, one needs to be aware of this bias through linearization. Still, it neither affects the essence of the analysis nor the magnitudes of temperature change in significant ways.

This part of the analysis demonstrates distinctly how different radiative forcings affect temperature development. While the absolute variables portray different biases, they capture topographic dependencies of temperature and radiative fluxes. When it comes to differences from the change period 1991-2020 compared to the reference period 1961-1990, the simulations do not capture the observed spatial variation of change. Further, they significantly underestimate the increase of net solar radiation so that this part of the radiative forcing nearly disappears. This leads to an underestimation of temperature increase in both simulations, especially in MPI-LR/REMO2009.

5 Discussion

5.1 Limitations

This analysis is subject to certain limitations which are discussed in this section.

This evaluation offers a comparison of 30-year climatological means over the whole period with a focus on spatial distributions. Seasonal differences have been neglected and so has the temporal development of the variables. This also means that extreme events are not part of this analysis. Further, variables outside of radiative fluxes and temperature have not been taken into account.

Several errors in the observations cannot be excluded due to measurement uncertainties and assumptions in computations. There might be a slight bias through the placement of weather stations that provide the observations, e.g. temperatures in cities might deviate from nearby less urbanized regions. Through the interpolation between the weather stations and filling in of data through reanalysis datasets, there might be systematic regional inaccuracies. When regridding the dataset to the same grid as the simulations for comparability, it is possible that small biases occurred, e.g. in the magnitude of 0.01 K for air temperature, which is negligible. Further, through the assumption of a constant albedo 15 %, differences in albedo and hence net solar radiation R_s linked to different kinds of land cover, such as forest or urban areas, might have been neglected.

In downwelling longwave radiation, more uncertainties could occur. While none of the variables can be considered completely independent from each other, downwelling longwave radiation $R_{ld, Brutsaert}$ is directly linked to temperatures through Brutsaert, i.e. a change or a temperature error will directly affect R_{ld} in DWD-HYRAS. When adjusting $R_{ld, Brutsaert}$, the period 2001-2020 instead of the standard reference period needed to be used due to data availability which might have led to a small offset in the adjusted data. The assumption of a constant instead of spatially dependent relative offset of actual from computed R_{ld} radiation might have also led to loss of data or a systematic error. According to (Kato et al., 2018), the potential measurement error in downwelling longwave radiation in the CERES dataset is between 3 and 6 W/m^2.

Regarding the simulations, the chosen combinations of global and regional climate models merely represent two simulations out of the 55-model ensemble of EURO-CORDEX. This could limit the possibility of making general statements about climate model simulations. Still, they are among the more prominent models of the ensemble. According to the ReKliEs-DE results report (Hübener; Bülow, et al., 2018), the HadGEM-driven model appears to be at the higher end of the temperature spectrum both climatologically and regarding trends. The MPI-driven model is said to lay in the middle in terms of climatology and at the lower end of the spectrum in terms of trends. Hence, the two analyzed example simulations provide an interesting inview into the magnitude of climatological bias and the possible range of change in climate model simulations in the analyzed time scale over Germany.

In chapter A.3 in the appendix, all spatial means over the climatological periods have been portrayed with an accuracy of 0.01 K and 0.01 W/m^2. However, the described uncertainties hint at an accuracy of 0.1 K for temperatures and temperature differences and 1 W/m^2 for radiative fluxes and their differences.

To conclude, in terms of variables and measurements, the comparison might have been limited due to differences in the grid between the observations and simulations, different assumptions on albedo and several necessary steps to acquire R_{ld} in the observations. Further, interdependencies between the variables have not been taken into account. The accuracy of results can be limited due to the use of the surface energy balance, since I use it to determine changes in surface temperature and relate these to

changes in air temperature. This may cause a bias since surface temperature reacts more strongly to radiation change than air temperature (Panwar et al., 2019). Additionally, the linearization of the surface energy balance with fixed initial temperature does not reflect the change of climate sensitivity over time and through temperature increase which can cause a bias in the surface temperature change itself. Further, I assume the turbulent (upwelling) fluxes operate at the maximum power limit. Deviations from that limit might add to the uncertainty.

However, these limitations don't restrict the key takeaways of this analysis and their necessary fulfilled conditions in significant ways. The analysis shows that air temperature and surface temperature agree very well in climatological time scales and air temperature changes can be used to support computations of surface temperature changes. The approximation of turbulent fluxes working at the maximum power limit seems to represent very well the actual fluxes. The regional differences, especially of R_s, can be interpreted with the possible restricted spatial distribution in mind. The possible uncertainty in R_ld appears to be minor given the noticeable agreement of T_surface diagnosed via the energy balance and T_air from the dataset. The chosen set of climate model simulations and associated projections can be considered representative under reservation.

5.2 Interpretations

I will first discuss the prominent results or possible incongruencies in the analysis of the climatological bias over the reference period. Then I will go on to the comparison between the change and reference period, and between the observed and simulated changes, and discuss interdependencies between the two regarding temperature and radiative fluxes. From that, temperature responses to radiative forcings are analyzed.

5.2.1 Climatological bias

In terms of spatial distribution of air temperature, both simulations capture the regional differences according to topographic differences. The consequences of altitude differences are well represented with elevated or mountainous areas. Valleys and flatter areas show lower temperatures and also experience a slight decrease toward the north. In the spatial mean over Germany, both simulations portray a slight positive air temperature bias of approximately 0.6 K in HadGEM/REMO2015 and 0.4 K in MPI/REMO2009. This aligns with the ReKliEs-DE results report where it is stated – given that general temperature bias is determined by the driving GCM – that the GCM HadGEM2 is at the higher end of the temperature spectrum and GCM MPI-LR is in the middle. Since there is no further reference in this analysis to show the full range of the possible air temperature bias, I can only confirm that the bias in HadGEM2 is stronger than the one in MPI-LR. This suggests a general slight positive air temperature bias in climate model simulations which would need to be backed up by more evaluations, especially of GCMs listed in the lower section of the temperature range. An analysis of the influence of RCM choice on the temperature bias exceeds the scope of this work.

In net solar radiation, the simulations portray similar general geographic distribution patterns while one simulation shows a positive bias over the spatial mean.

The spatial distribution shows a general pattern of increase in mean net solar radiation from north to south which is consistent with the observations. However, the spatial differences are more pronounced in the simulations than in the observations and seem to correspond very strongly to topographic differences

that are not reflected to the same extent in the observations. Partly, the different assumptions on albedo might affect the spatial distribution but they cannot fully explain where this deviation comes from. This could indicate that in the simulations, net solar radiation mainly depends on latitude and altitude. Other factors might be projected differently, such as cloud cover, that also strongly affect absorbed solar radiation. To support this hypothesis, a more detailed analysis would be necessary.

In net solar radiation, HadGEM2/REMO2015 shows a strong positive bias of approx. $7\,\mathrm{W/m^2}$ from the observations averaged over Germany. MPI-LR/REMO2009 shows a slight negative offset of less than $1\,\mathrm{W/m^2}$. According to (Vautard et al., 2021), this bias is mostly dominated by the RCM choice.

In downwelling longwave radiation, the biases are smaller than in net solar radiation. All three datasets show similar regional differences that can be mostly attributed to elevation differences. Over elevated regions, solar radiation increases due to less absorption and scattering in the atmospheric column. Downwelling longwave radiation decreases with height since temperatures are decreasing, allowing less water vapor content and hence reducing possible particles to contribute to the radiative flux (DWD, [n.d.]).

Incoming and outgoing long-wave radiation decrease both with increasing height particularly in the first 1000 metres due to decreasing temperatures and water vapor content as shown in the figure.

Examining the two considered types of radiative fluxes, one can see that the spatial patterns are rather accurately opposed to each other regarding local differences across all three datasets. Net solar radiation is stronger over elevated regions and downwelling longwave radiation is stronger over lower regions. This is due to the opposed restrictions on radiation: net solar radiation is restricted by e.g. aerosols and clouds, hence a smaller atmospheric column can lead to enhanced shortwave flux. Downwelling longwave radiation is restricted by the possible space in the atmospheric column for greenhouse gases, leading to an opposite effect as in net solar radiation.

I use the surface energy and maximum power to diagnose surface temperatures. They both combined reconstruct temperature very well. This implies that over the 30-year time scale, where diurnal changes are not taken into account, the discrepancies between air and surface temperature can be neglected. This is well reflected in the simulations. The scattering of surface temperature compared to air temperature might be linked to the enhanced regional solar radiation variation in the simulations that I already discussed. Overall, it is minor given the temperature magnitude in Kelvin.

While the resulting surface temperature is – apart from the slight bias – in the same magnitude, the radiative fluxes behind it show a discrepancy. The positive bias of net solar radiation in HadGEM2/REMO2015 seems to be cancelled out by the smaller negative bias in downwelling longwave radiation. This can be explained by turbulent fluxes working at the maximum power limit, implying that the impact of differences in net solar radiation weighs half as much as a difference in downwelling longwave radiation. The bias in R_s is approximately twice as big as the one in R_ld which aligns with the described cancelling out of biases. Differences in baseline radiation values to reproduce climatology may lead to nearly the same temperature result. However, this discrepancy might lead to completely different hydrological cycle responses (Kleidon; Kravitz, et al., 2015) that are not part of this analysis but might need to be assessed in more detail. Hence, it is crucial to consider more than only temperature as a variable when evaluating climate change in simulations even if it initially indicates similarity.

The simulations' bias in surface temperature is hence similar to the bias in air temperature. This might lead to a bias in climate sensitivity to both examined radiative forcings. With higher initial temperature,

the climate sensitivity to radiative forcings might decrease, meaning that temperature responses to the same radiative change can turn out weaker. To estimate climate sensitivity would be a different analysis.

5.2.2 Air temperature and radiation change bias

In the change analysis, it becomes clear at the beginning that temperature increase is underestimated by the simulations.

In the observed temperature change, regional patterns of change can be noticed. This seems to be partly linked to topographic differences and, as noted, different forms of land use, i.e. urbanized areas such as the one around Berlin heat faster than others (Liu et al., 2022). In the simulations, the temperature increase shows little to no spatial differences which could indicate that certain elements of the surface energy balance are not or differently taken into account at regional scale. Averaged over Germany, the temperature increase is strongly underestimated by the simulations, which was the motivation behind this analysis in the first place.

The explanation for this general discrepancy is directly provided through the next part of this work.

In net solar radiation, the DWD-HYRAS observations show an increase of radiative flux in the magnitude of 4 W/m^2 with pronounced regional differences. Especially in the area in and around Saxony, R_s portrays stronger increase than in any other region. The first possible and common reason for this exacerbated increase could be linked to a decrease in aerosols in the atmosphere. There are indications that the aerosol reduction was the key driver for net solar radiation increase in Europe only until 2002 and after that, cloud cover reduction was the most prominent reason for increasing solar radiation (Schilliger et al., 2024 (under revision)).

This increase in solar radiation can not be found in the simulations. Both show less spatial differences in net solar radiation change. This could indicate that either aerosol reduction or cloud cover change or both might be neglected or differently projected by the simulations. In Western Europe, underestimated net solar radiation increase and hence temperature increase was already attributed to neglected aerosol changes (Schumacher et al., 2024) with which this analysis could be consistent as well. Further, models with a strong temperature increase seem to portray little to no reduction in solar radiation (this is referred to as radiation global in the according analysis) while those with smaller temperature increase show stronger shortwave flux reduction (Hübener; Bülow, et al., 2018). This link between strong and weak temperature change and solar radiation change could indicate that, while the RCM choice is relevant for the baseline solar radiation in the models, the GCM choice dictates its magnitude and direction of change.

The downwelling longwave radiation change in the observations is in the same magnitude of net solar radiation change, i.e. 4 W/m^2. Its spatial distribution contrasts the change of net solar flux change which is consistent with the aforementioned properties and restriction of both radiative fluxes. Despite a narrower range, the simulations show the same magnitude of change. Here, the difference in downwelling long-wave radiation between the RCP scenarios is more pronounced than the one in solar radiation was. This is due to the RCP scenarios describing mostly greenhouse gas emission developments that directly affect R_{ld}.

The accurate alignment of topographic differences in climatology but not in changes could indicate on the one hand that the regionalization of the climate models does not affect the changes as strong as it affects climatology. On the other, the driving global climate model might not reflect topography to an extent where regional differences become prominent.

5.2.3 Temperature responses

As indicated in the previous sections, both the initial climatology and the different radiative flux changes impact temperature development. In the observations, the initial temperature is slightly lower than in the simulation, leading to a slightly more expressed temperature response overall. The observed net solar radiation increase is way higher than the simulations capture, hence the temperature response to this radiation change is enhanced. Accordingly, in the simulations, the already small net solar radiation change leads to a smaller temperature change in proportion to it.

Apart from regional differences, the magnitude of warming attributed to downwelling longwave radiation change is similar between the observations and simulations. The slight overestimation can be attributed to the chosen RCP. This could indicate that potentially RCP8.5 overestimates the increase in downwelling longwave radiation to a small extent. On account of only half of the change period including projection data, I cannot make a well-founded statement about this.

Due to maximum power, the effect of net solar radiation change is half as big as of downwelling longwave radiation change. Since in DWD-HYRAS, both radiative changes lay in the same magnitude, the impact of R_s makes up for approx. one-third of warming in the observations. The missed temperature change in the simulations is within 20 to 40 % which aligns well with one third of warming being neglected.

An additional inference that has not been taken into account yet is that when net solar radiation increases, it might be due to less cloud cover. Less cloud cover might imply enhanced climate sensitivity to CO_2 and other greenhouse gases apart from water vapor since the atmospheric window is closed in fewer regions or for shorter times (Stevens et al., 2023).

5.3 Implications

Several implications can be derived from this.

1. In Germany, climate model simulations underestimate temperature changes due to missed solar radiation trends. This might imply further underestimation of warming in the future.

2. The weaker increase in R_s that might be due to insufficiently projected cloud cover decrease could further entail stronger impact of CO_2 and CO_2 equivalent emissions on temperature increase.

3. The importance of not only taking greenhouse effect into account but other radiative forcings as well is once more emphasized.

4. The importance of taking into account radiative fluxes behind temperature reconstruction is highlighted since consequences for the hydrologic cycle might deviate.

5. The surface energy balance with maximum power can be used as an adequate tool to describe temperature and temperature change at climatological time scales and regional grid scales solely based on net solar and downwelling longwave radiation in the atmospheric column.

6 Summary and Outlook

In this analysis, I compared the temperature and radiative flux output of two EURO-CORDEX simulations with DWD-HYRAS observations over Germany for the climatological reference period 1961-1990 and the developments from there to the change period 1991-2020. Three key takeaways emerged from this analysis:

1. The surface energy balance and maximum power adequately portray temperature and temperature changes in Germany and is consistent within observations and the examined EURO-CORDEX simulations.

2. Climate model simulations show a more uniform trend in spatial distribution in temperature and radiative fluxes than observed in Germany from 1961 to 2020.

3. Climate model simulations underestimate the already observed warming in Germany because they significantly underestimate net solar radiation increase. Downwelling longwave radiation change is not underestimated.

Both hypotheses from the beginning of this analysis can be confirmed.

This work provided me with deep insight into climate models and radiative forcings. It opens up a broad range of possible further analysis. In particular, treating these climate model simulations, further analysis of the temporal development of average temperatures and their spatial distribution could provide an interesting in-view. A comparison of seasonal changes could be intriguing to examine the temporal uniformity or irregularities of temperature and radiation change.

A Appendix

A.1 Variables and Abbreviations Dictionary

Here, all relevant abbreviations and variables of this work can be found, ordered by apparition in the text.

Abbreviation	Meaning
IPCC	Intergovernmental Panel on Climate Change
CORDEX	Coordinated Regional Climate Downscaling Experiment
CMIP5	Coupled Model Intercomparison Project 5
EURO-CORDEX	European branch of CORDEX
ReKliEs-DE	Regionale Klimaprojektionen Ensemble Deutschland
DWD	Deutscher Wetterdienst
RCP	Representative Concentration Pathway
GCM	global climate model
RCM	regional climate model
DWD-HYRAS	DWD Hydrometeorological Raster Dataset
HadGEM2	HadGEM2-ES global climate model (UK)
REMO2015	GERICS-REMO2015 regional climate model (Germany)
MPI-LR	MPI-M-MPI-ESM-LR global climate model (Germany)
RMSE	Root mean squared error

Table A.1: Overview of used abbreviations ordered by apparition in this work.

Variable	Meaning
R_s	Net shortwave (solar) radiation at surface
R_{ld}	Downwelling longwave (thermal) radiation (greenhouse effect)
σ	Stefan-Boltzmann constant ($5.67 \cdot 10^{-8}$ W/(m$^2 \cdot$K))
$T_{Surface}, T_s$	Surface temperature
J	Turbulent fluxes
R_{sd}	Downwelling shortwave (solar) radiation
α	Surface Albedo
T_i	Temperature in reference period
$(\Delta T_s)_{solar}$	Temperature response to net solar radiation change
$(\Delta T_s)_{ld}$	Temperature response to downwelling longwave radiation change
α_{HYRAS}	assumed surface albedo in the DWD-HYRAS observations (15 %)
T_{air}	Air Temperature at 2 m height
$R_{ld,cs}$	Downwelling longwave (thermal) radiation for clear sky conditions
ε_{cs}	Clear sky emissivity of the atmosphere
e_a	2m water vapor pressure
RH	Relative humidity
e_s	saturation water vapor pressure
$R_{ld,Brutsaert}$	$R_{ld,cs}$ for the HYRAS dataset
$\alpha_{Simulations}$	surface albedo in the simulations
R_{su}	Upwelling shortwave (solar) radiation

Table A.2: Dictionary of used variables ordered by apparition in this work.

A.2 Color scheme

For the map plots, I consulted the IPCC Visual Style Guide for WGI Authors (Gomis et al., 2022). The used colormaps for the map plots are listed in table A.3. For the scatterplots, I consulted the Max Planck Corporate design manual (Max-Planck-Gesellschaft, 2022). The markers for each portrayed variable can be found in table A.4. The colors for the scatter plots have been assigned as follows:

- DWD-HYRAS: MPG dark blue: #29485d

- HadGEM/REMO2015: MPI orange: #ef7c00

- MPI/REMO2009: MPI logo green: #006c66

Map plots		
Portrayed variable	Color scheme in Matplotlib	Color bar
Absolute Temperature	YlOrBr − 16 steps	
Temperature change	RdBu_r − 17 steps	
Absolute Radiation	CMRmap_r − 16 steps	
Radiation Change	seismic − 17 steps	

Table A.3: Color scheme of map plots as inspired by the IPC visual style guide (Gomis et al., 2022).

Scatter plots				
Variable	marker	DWD-HYRAS	HadGEM2/REMO2015	MPI-LR/REMO2009
T_s, T_{air}; ΔT_s, ΔT_{air}	circle 'o'	○	○	○
R_s; ΔR_s	star '*'	none	★	★
R_{ld}; ΔR_{ld}	pentagon 'p'	none	⬠	⬠

Table A.4: Color scheme of scatter plots, colors chosen in MPG corporate design guide (Max-Planck-Gesellschaft, 2022).

A.3 Means and Standard Deviations of Relevant Variables

This section is a collection of spatial mean values over Germany of all relevant variables $\overline{Variable}$ and their standard deviation $\sigma(Variable)$. In table A.5, these values are collected for the climatological bias (section 4.1). In table A.6 the corresponding values to sections 4.2 and 4.3 can be found. All values have been rounded to two digits after the decimal point. The limitations of this analysis indicate an accuracy of 0.1 K in temperature data and of 1 W/m^2 in radiative fluxes.

Dataset	$\overline{Variable}$	$\sigma(Variable)$
Air temperature T_{air} (K)		
DWD-HYRAS	281.41	0.85
HadGEM2/REMO2015	281.97	0.70
MPI-LR/REMO2009	281.81	0.71
Net solar radiation R_s (W/m^2)		
DWD-HYRAS	97.60	5.30
HadGEM2/REMO2015	104.57	6.78
MPI-LR/REMO2009	96.86	5.59
Albedo α $(\%)$		
DWD-HYRAS	15	0
HadGEM2/REMO2015	15.13	1.10
MPI-LR/REMO2009	15.13	1.21
Downwelling longwave radiation R_{ld} (W/m^2)		
DWD-HYRAS	307.62	5.09
HadGEM2/REMO2015	305.80	5.84
MPI-LR/REMO2009	308.52	5.78
Surface temperature T_s (K) via surface energy balance		
DWD-HYRAS	281.52	0.81
HadGEM2/REMO2015	281.89	0.80
MPI-LR/REMO2009	281.67	0.78

Table A.5: Spatial means and standard deviation of relevant variables in the reference period 1961-1990.

Dataset	$\overline{Variable}$	$\sigma(Variable)$
Air temperature change ΔT_{air} (K)		
DWD-HYRAS	1.07	0.12
HadGEM2/REMO2015, RCP2.6	0.81	0.04
HadGEM2/REMO2015, RCP8.5	0.90	0.04
MPI-LR/REMO2009, RCP2.6	0.51	0.07
MPI-LR/REMO2009, RCP8.5	0.67	0.06
Net solar radiation change ΔR_s (W/m^2)		
DWD-HYRAS	4.33	1.37
HadGEM2/REMO2015, RCP2.6	0.43	0.76
HadGEM2/REMO2015, RCP8.5	0.93	0.67
MPI-LR/REMO2009, RCP2.6	-1.04	0.56
MPI-LR/REMO2009, RCP8.5	-0.84	0.45
Temperature response $\Delta T_{s,solar}$ to ΔR_s (K)		
DWD-HYRAS	0.43	0.13
HadGEM2/REMO2015, RCP2.6	0.04	0.07
HadGEM2/REMO2015, RCP8.5	0.09	0.07
MPI-LR/REMO2009, RCP2.6	-0.10	0.06
MPI-LR/REMO2009, RCP8.5	-0.08	0.04
Net downwelling longwave radiation change ΔR_{ld} (W/m^2)		
DWD-HYRAS	4.21	0.87
HadGEM2/REMO2015, RCP2.6	4.36	0.28
HadGEM2/REMO2015, RCP8.5	4.61	0.21
MPI-LR/REMO2009, RCP2.6	3.58	0.42
MPI-LR/REMO2009, RCP8.5	4.47	0.47
Temperature response $\Delta T_{s,ld}$ to ΔR_{ld} (K)		
DWD-HYRAS	0.83	0.17
HadGEM2/REMO2015, RCP2.6	0.86	0.06
HadGEM2/REMO2015, RCP8.5	0.91	0.04
MPI-LR/REMO2009, RCP2.6	0.71	0.08
MPI-LR/REMO2009, RCP8.5	0.88	0.09
Diagnosed surface temperature change ΔT_s (K)		
DWD-HYRAS	1.26	0.14
HadGEM2/REMO2015, RCP2.6	0.90	0.06
HadGEM2/REMO2015, RCP8.5	1.00	0.06
MPI-LR/REMO2009, RCP2.6	0.60	0.11
MPI-LR/REMO2009, RCP8.5	0.80	0.09

Table A.6: Spatial means and standard deviation of change of relevant variables between the two periods 1991-2020 and 1961-1990.

A.4 Albedo in Euro-CORDEX Simulations
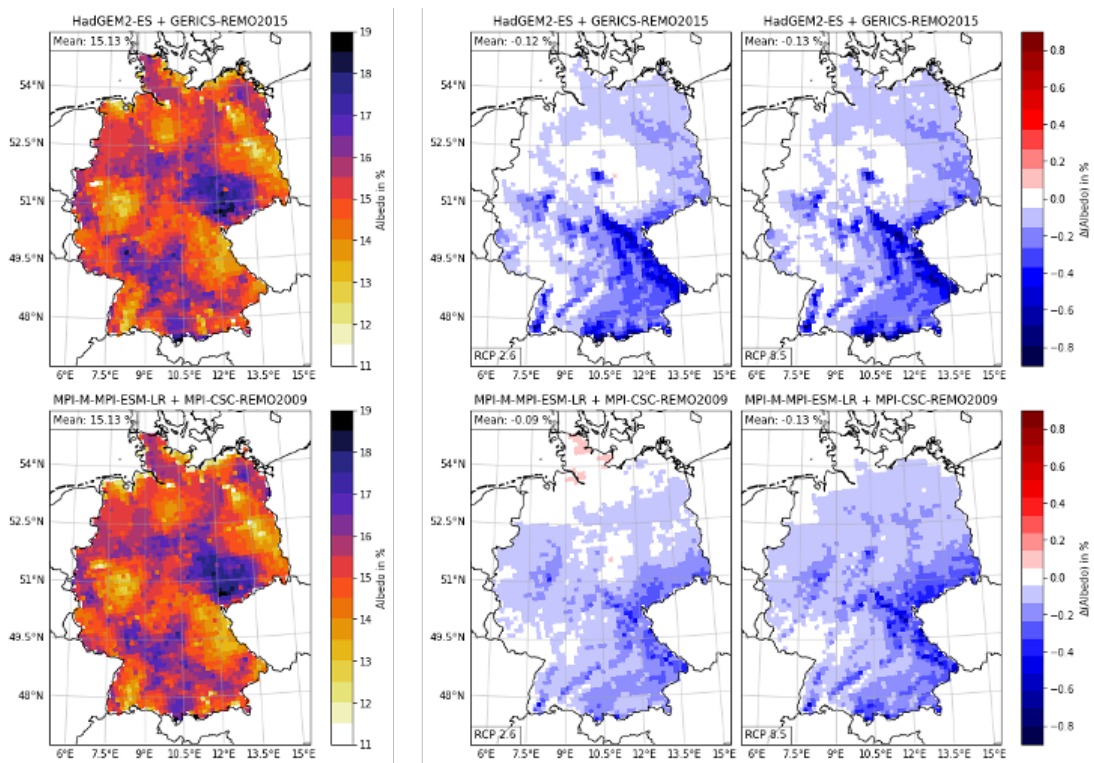
Figure A.1: Mean albedo in reference period 1961-1990 (left) and albedo change with RCP 2.6 (middle) and RCP 8.5 (right) in simulations HadGEM/REMO2015 (top row) and MPI/REMO2009 (bottom row). Spatial mean (top left corner) and Scenario (bottom left corner) included.

The albedo in Germany in the reference period and albedo change separated by RCP scenario is portrayed In figure A.1. Neither in terms of magnitude nor in terms of spatial variation do the two datasets deviate from one another in significant ways. Both portray a slight decrease in albedo between the two periods, especially in mountainous regions towards the south-east. This might be related to decreasing snow cover during winter, but a detailed evaluation of this hypothesis exceeds the framework of this work and my, the author's, emotional capacities. The noticeable spatial variability in albedo between 12 and 18 % leads to slightly higher spatial variability of net solar radiation in the simulation data compared to the observational data where albedo is assumed to be 15 %.

A.5 Adjusting downwelling longwave Radiation in DWD-HYRAS
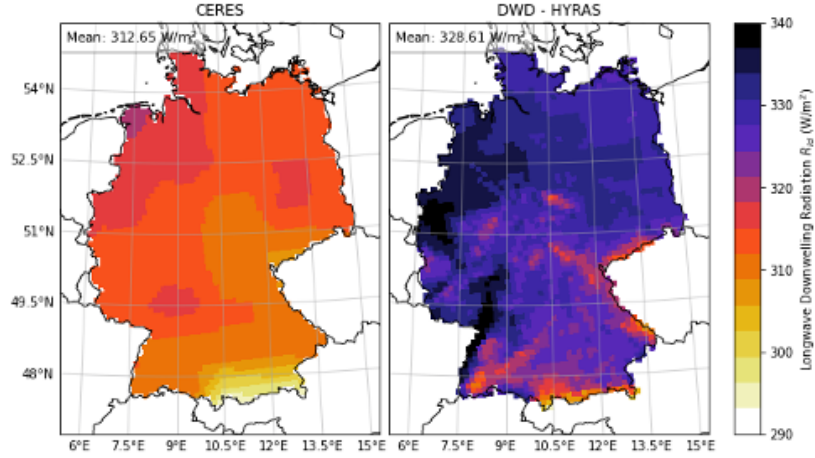
Figure A.2: downwelling longwave Radiation over Germany in 2001-2020, in CERES satellite observations and from DWD-HYRAS via Brutsaert.

Downwelling longwave radiation R_{ld} (W/m^2) **(2001-2020)**		
Dataset	Spatial mean (W/m^2)	Standard deviation (W/m^2)
DWD-HYRAS (Brutsaert)	328.61	5.13
CERES	312.65	3.37

Table A.7: Spatial mean and standard deviation for downwelling longwave radiation R_{ld} in DWD-HYRAs diagnosed via Brutsaert equation and from CERES satellite observations.

In the DWD-HYRAS dataset, downwelling longwave radiation R_{ld} is not directly available. Thus, it was diagnosed via Brutsaert (Brutsaert, 1975 and Tian et al., 2023) through humidity and air temperature. The deriving of R_{ld} was not part of this work but was already performed by my second supervisor Dr. Axel Kleidon who made this data available to me. Due to the clear-sky assumptions mentioned in the corresponding Methods section (3.3.1), the diagnosed values for downwelling longwave radiation show a consistent positive bias from the realistic magnitude. To estimate this magnitude, CERES satellite observations have been taken into account (NASA-CERES, 2024).

The satellite observations are provided from the beginning of 2001 and DWD-HYRAS humidity data end in 2020. Hence, the period of 2001-2020 has been used for the correction. Figure A.2 portrays the spatial distribution over Germany of R_{ld} in CERES and DWD-HYRAS via Brutsaert. Since CERES uses a grid size of $1° \times 1°$, the dataset was regridded to the CORDEX grid for masking.

In fig. A.2, one can see that CERES data shows significantly less spatial variability. To conserve the spatial distribution due to topographic differences inherent in the dataset for humidity and air temperature, a constant relative offset was assumed and determined to be

$$\mathrm{mean}\left(\frac{R_{\mathrm{ld,\,CERES}}}{R_{\mathrm{ld,\,DWD}}}\right) = 0.95 \pm 0.01\,. \tag{A.1}$$

The factor 0.95 was used to adjust R_{ld} in the observational data.

A.6 Scatterplots of climatological biases in the reference period

(a) Air temperature T_{air}

(b) Net solar radiation R_{s}

(c) Downwelling longwave radiation R_{ld}
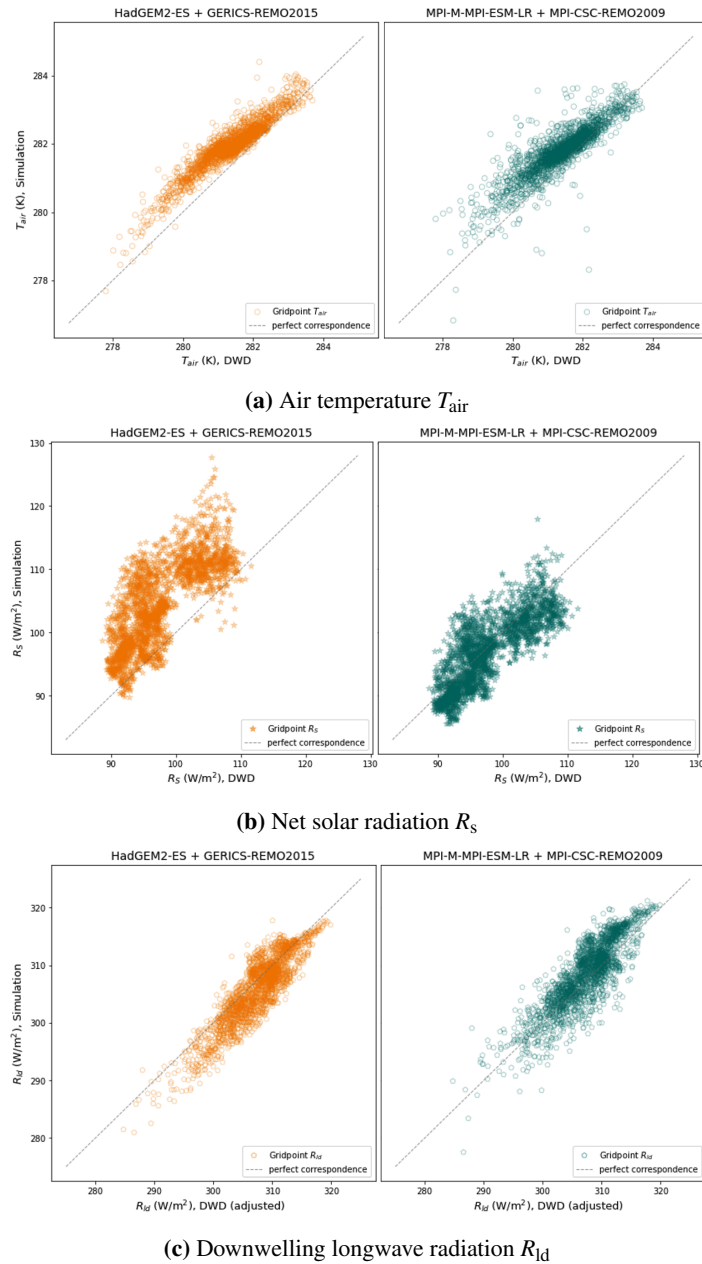
Figure A.3: Scatterplots for climatological bias over the reference period in air temperature (top row), net solar radiation (middle row) and downwelling longwave radiation (bottom row) in the climate model simulations HadGEM/REMO2015 (left) and MPI/REMO2009 (right) plotted over the corresponding observation data of the DWD-HYRAS dataset.

Here, the corresponding scatter plots to the maps in figure 4.1 are portrayed. They visualize the findings from the map plots in a different way, showing the scattering of the biases. The discussed stronger spatial differences in net solar radiation in the simulations compared to the observations are illustrated once more in figure A.3b.

A.7 Change biases and RCP 2.6

Air temperature change
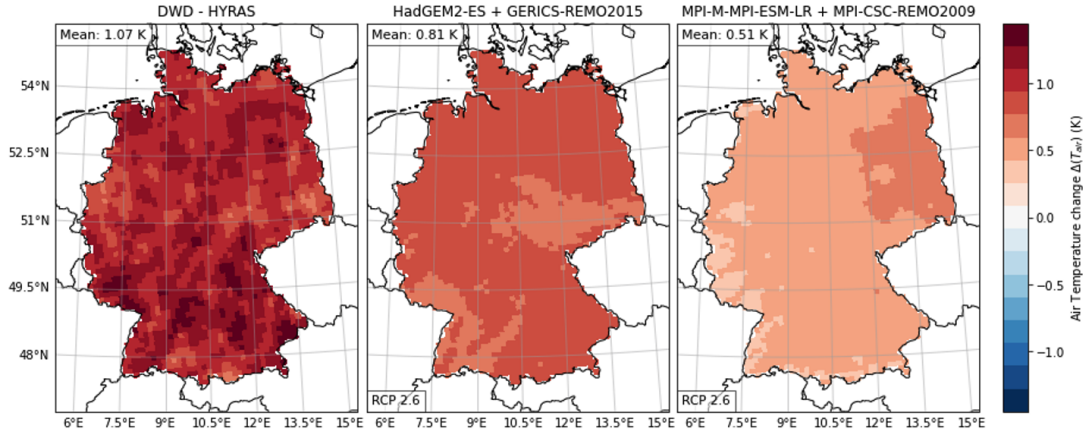
Figure A.4: Air Temperature difference between period 2 (1991-2020) and period 1 (1961-1990) in observations (left) and simulations HadGEM/REMO2015 (middle) and MPI/REMO2009 (right) with RCP 2.6 projections, spatial mean over Germany included (top left corner of each map).
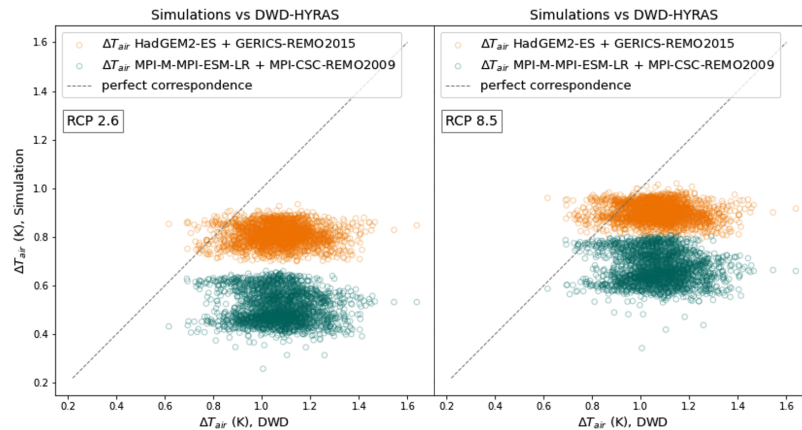
Figure A.5: Scatter plot of air temperature change ΔT_{air} in simulations plotted over ΔT_{air} in observations, perfect correspondence line and scenario included (top left corner)

Figure A.4 shows maps of the air temperature change in observations and simulations with RCP2.6. The general findings are the same as in in figure 4.3, but the negative bias against the observations is bigger.

In figure A.5, the air temperature change bias of the simulations compared to the DWD-HYRAS observations is portrayed, supporting the maps in figures 4.3 and A.4.

Radiation change and temperature response
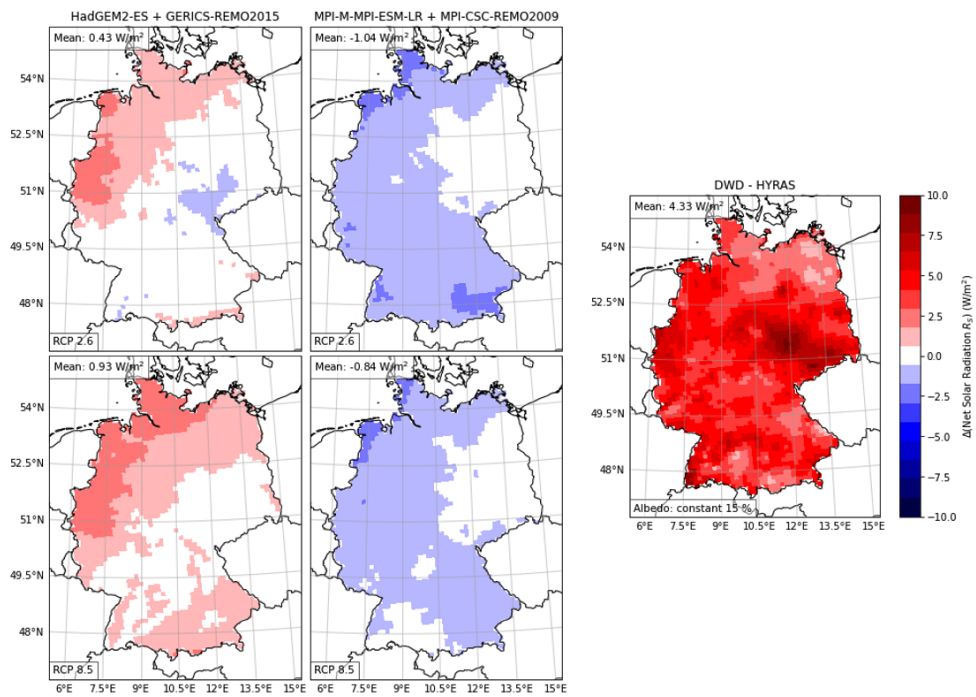
(a) Net solar radiation difference ΔR_s.
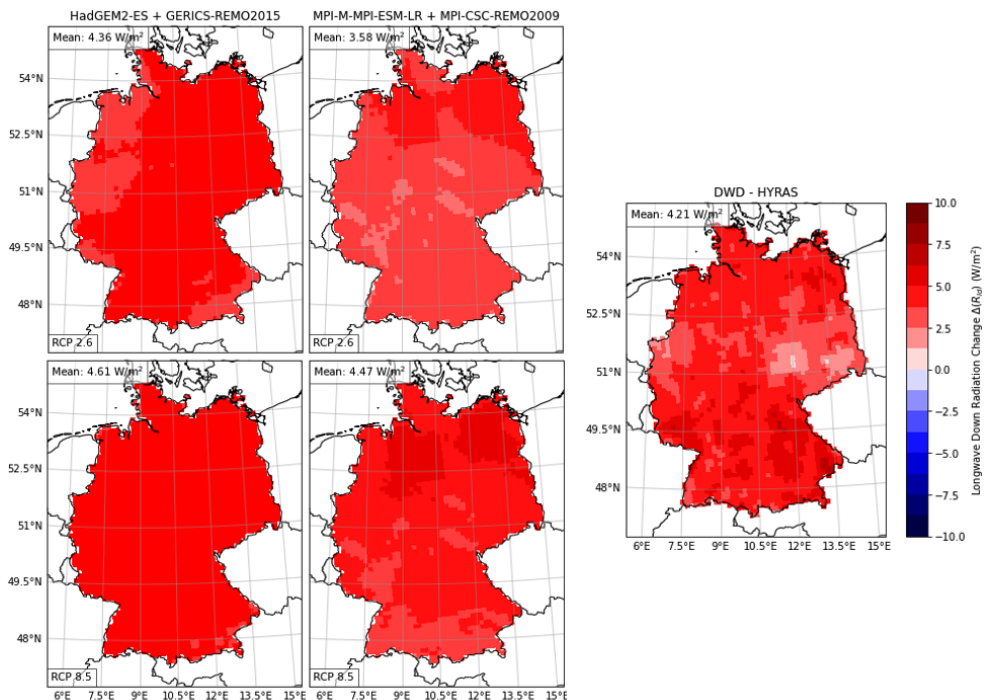
(b) Downwelling longwave radiation difference ΔR_{ld}.

Figure A.6: Net solar (top figure) and downwelling longwave (bottom figure) radiation differences between periods 1961-1990 and 1991-2020 in observations (right) and simulations HadGEM/REMO2015 (left) and MPI/REMO2009 (middle) for RCP2.6 (top row) and RCP8.5 (bottom row).
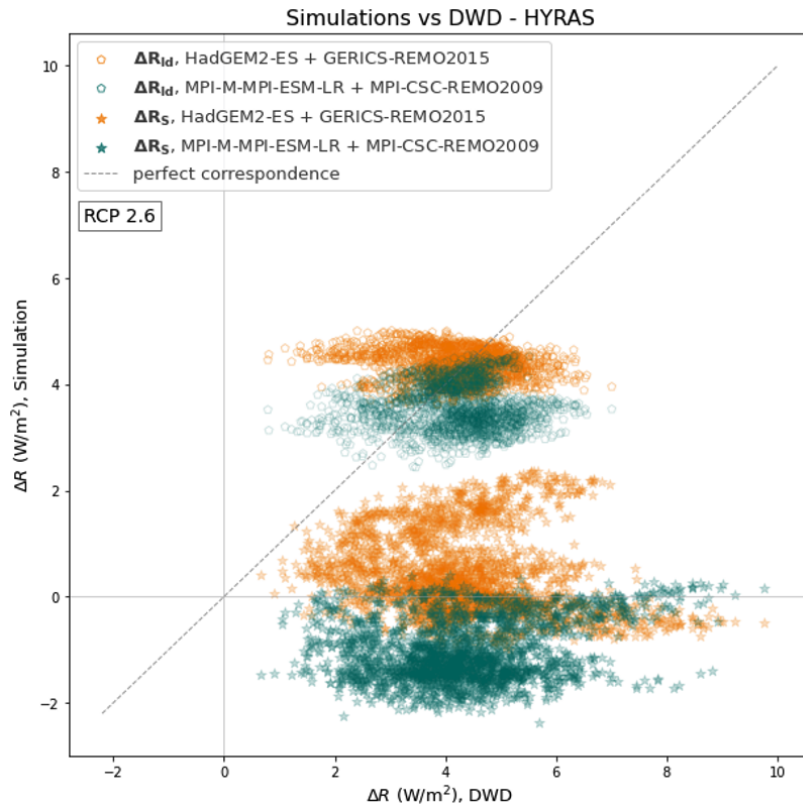
Figure A.7: Mean net solar and downwelling longwave radiation change between period 2 (1991-2020) and period 1 (1961-1990) from simulations (RCP2.6) plotted against observed trends for each gridpoint, perfect correspondence line included.

In figure A.6, net solar and downwelling longwave radiation changes (radiative forcings) in all three datasets are portrayed. This visualizes further the findings in figure 4.4 from chapter 4.2 over the map of Germany. One can see the significant regional differences in the increase of radiative fluxes in the observations that are not captured by the simulations.

Figure A.7 shows the simulations' radiation change distribution. Both radiative changes are similarly distributed as in figure 4.4 but one can see that in HadGEM/REMO2015, more gridpoints of ΔR_s are gathered below zero, hence show a decrease. This might imply that over time and with more drastic scenarios, R_s still increases in the simulations but still is not captured to the observed extent.
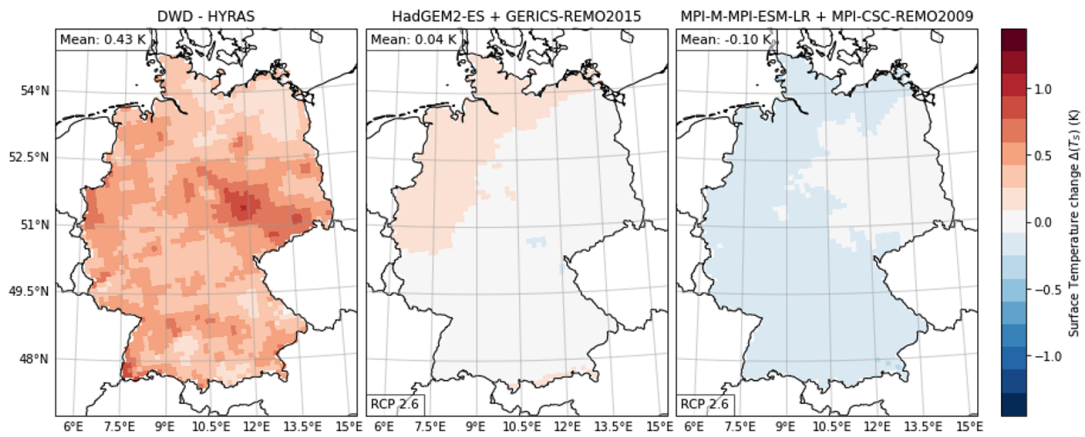
(a) Surface temperature response to net solar radiation change.
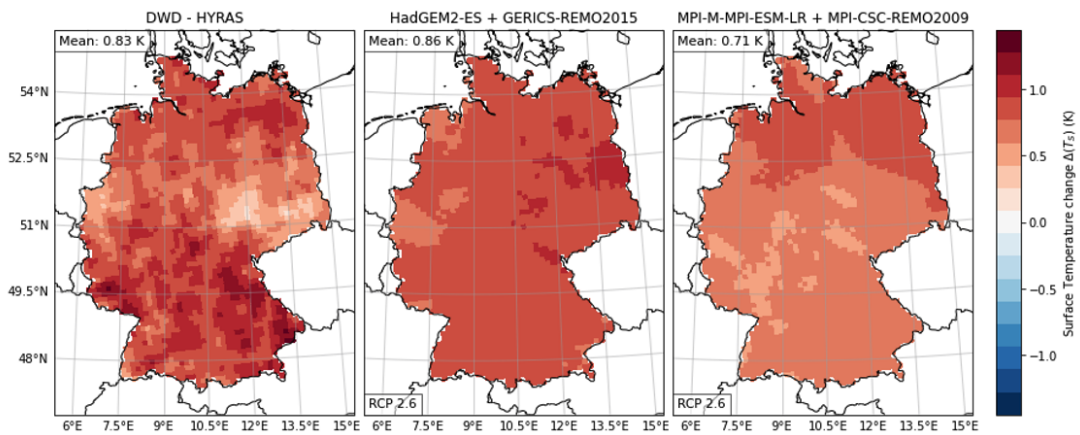
(b) Surface temperature response to downwelling longwave radiation change

Figure A.8: Surface temperature response to radiative forcings by net solar radiation (top row) and downwelling longwave radiation (bottom row). change in observations (left) and HadGEM/REMO2015 (middle) and MPI/REMO2009 (right) climate model simulations for RCP2.6 from the reference period 1961-1990 to the change period 1990-2020 over Germany, spatial ~~mean~~ nice (upper left corner of graph) and scenario included (bottom left corner).

In figure A.8, one can see that in both simulations, the temperature response to ΔR_s is also weaker than in RCP8.5. In MPI/REMO2009 it decreases slightly stronger than in the other scenario, suggesting that a more drastic scenario in that simulation would not lead to more loss of R_s but rather to less, potentially turning into an increase in future projections.

List of Figures

List of Tables

References

BENESTAD, Rasmus; BUONOMO, Erasmo, et al., 2021. *EURO-CORDEX Guidelines Version 1.1 - 2021.02: Guidance for EURO-CORDEX climate projections data use*. EURO-CORDEX community. Version 1.1. Published by the EURO-CORDEX community, Additional contributor: András Horányi (C3S).

BRUTSAERT, Wilfried, 1975. On a derivable formula for long-wave radiation from clear skies. *Water Resources Research*. Vol. 11, no. 5, pp. 742–744.

BUDYKO, M. I., 1969. The effect of solar radiation variations on the climate of the Earth. *Tellus*. Vol. 21, no. 5, pp. 611–619.

CAI, Jun, 2019. *Humidity measures*.

COPERNICUS CLIMATE CHANGE SERVICE, 2019. *Climate Data Store, CORDEX regional climate model data on single levels* [online]. [visited on 2024-05-01]. Available from: `https://cds.climate.copernicus.eu/`. Copernicus Climate Change Service (C3S) Climate Data Store (CDS).

DWD, 2018. *Wetter und Klima - Deutscher Wetterdienst - Datensätze auf der Basis der RCP-Szenarien*.

DWD, 2020a. *Raster data set of daily mean global radiation in W/m^2 for Germany - HYRAS-DE-RSDS, Version v3.0*. Frankfurter Str 135, 63067 Offenbach am Main: Deutscher Wetterdienst Hydrometeorologische Beratungsleistungen. Version v3.0. Dataset-ID: urn:x-wmo:md:de.dwd.cdc::GRD_DEU_P1D_RAD-G_HYRAS-DE.

DWD, 2020b. *Raster data set of daily mean relative humidity in % for Germany - HYRAS-DE-HURS, Version v5.0*. Frankfurter Str 135, 63067 Offenbach am Main: Deutscher Wetterdienst Hydrometeorologische Beratungsleistungen. Version v5.0. Dataset-ID: urn:x-wmo:md:de.dwd.cdc::GRD_DEU_P1D_RH_HYRAS-DE.

DWD, 2020c. *Raster data set of daily mean temperature in °C for Germany - HYRAS-DE-TAS, Version v5.0* [Dataset]. Frankfurter Str 135, 63067 Offenbach am Main: Deutscher Wetterdienst Hydrometeorologische Beratungsleistungen. Dataset-ID: urn:x-wmo:md:de.dwd.cdc::GRD_DEU_P1D_T2M_HYRAS-DE.

DWD, 2020d. *Wetter und Klima - Deutscher Wetterdienst - Leistungen - HYRAS - Hydrometeorologische Rasterdaten*. Deutscher Wetterdienst Hydrometeorologische Beratungsleistungen.

DWD, [n.d.]. *Wetter und Klima - Deutscher Wetterdienst - Radiation Processes - Vertical soundings of the radiative fluxes*.

GOMIS, Melissa I.; PIDCOCK, Roz, et al., 2022. *IPCC Visual Style Guide for WGI Authors*.

HÜBENER, Heike; BÜLOW, Katharina, et al., 2018. *ReKliEs-De Ergebnisbericht*.

HÜBENER, Heike; SPEKAT, Arne, et al., 2018. *ReKliEs-De Nutzerhandbuch*.

INTERGOVERNMENTAL PANEL ON CLIMATE CHANGE (IPCC), 2023. *Climate Change 2023: Synthesis Report. Contribution of Working Groups I, II and III to the Sixth Assessment Report of the Intergovernmental Panel on Climate Change*. Ed. by CORE WRITING TEAM, H. LEE AND J. ROMERO. Geneva, Switzerland: IPCC. Sections.

IPCC WORKING GROUP I, 2021. *Annex VII: Glossary, in Climate Change 2021: The Physical Science Basis. Contribution of Working Group I to the Sixth Assessment Report of the Intergovernmental Panel on Climate Change*. Cambridge University Press. Tech. rep.

KASPAR, Frank; FRIEDRICH, Karsten, et al., 2023. Observed temperature trends in Germany: Current status and communication tools. *Meteorologische Zeitschrift*. Vol. 32, no. 4, pp. 279–291.

KATO, Seiji; ROSE, Fred G., et al., 2018. Surface irradiances of Edition 4.0 clouds and the Earth's Radiant Energy System (CERES) Energy Balanced and Filled (EBAF) data product. *Journal of Climate*. Vol. 31, no. 11, pp. 4501–4527.

KLEIDON, Axel; KRAVITZ, Ben, et al., 2015. The hydrological sensitivity to global warming and solar geoengineering derived from thermodynamic constraints. *Geophysical Research Letters*. Vol. 42, no. 1, pp. 138–144.

KLEIDON, Axel; RENNER, Maik, 2018. Diurnal land surface energy balance partitioning estimated from the thermodynamic limit of a cold heat engine. *Earth System Dynamics*. Vol. 9, pp. 1127–1140.

KLIMA, Helmholtz, 2023. *What is climate sensitivity?*

LIU, Zihan; ZHAN, Wenfeng, et al., 2022. Surface warming in global cities is substantially more rapid than in rural background areas. *Communications Earth & Environment*. Vol. 3, no. 1.

MAX-PLANCK-GESELLSCHAFT, 2022. *Corporate Design Manual*. Max-Planck-Gesellschaft. Version 1.2.

NASA-CERES, 2024. *CERES EBAF TOA and Surface Fluxes: Monthly Averages and 07/2005 to 06/2015 Climatology*. Edition 4.2. Revised data release date: January 2, 2024. Climatology from 07/2005 to 06/2015. Conventions: CF-1.4.

NATIONAL OCEANIC AND ATMOSPHERIC ADMINISTRATION, 2023. *The Earth-Atmosphere energy balance*.

PANWAR, Annu; KLEIDON, Axel, et al., 2019. Do Surface and Air Temperatures Contain Similar Imprints of Evaporative Conditions? *Geophysical Research Letters*. Vol. 46, no. 7, pp. 3802–3809.

PFEIFER, S.; RECHID, D., et al., 2020. *Klimaausblick Deutschland* [Climate Service Center Germany (GERICS)]. Version 1.2, März 2021.

SCHILLIGER, Linda; TETZLAFF, Anke, et al., 2024. An investigation on causes of the detected surface solar radiation brightening in Europe using satellite data. *Authorea (Authorea)*.

SCHULZWEIDA, Uwe, 2016. *Climate Data Operators*. Version 1.7.2. Max Planck Institute for Meteorology. MPI for Meteorology.

SCHUMACHER, D.L.; SINGH, J., et al., 2024. Exacerbated summer European warming not captured by climate models neglecting long-term aerosol changes. *Commun Earth Environ*. Vol. 5, p. 182.

STEVENS, B.; KLUFT, L., 2023. A colorful look at climate sensitivity. *Atmospheric Chemistry and Physics*. Vol. 23, no. 23, pp. 14673–14689.

TIAN, Y.; ZHONG, D., et al., 2023. Understanding variations in downwelling longwave radiation using Brutsaert's equation. *Earth System Dynamics*. Vol. 14, no. 6, pp. 1363–1374.

VAUTARD, Robert; KADYGROV, Nikolay, et al., 2021. Evaluation of the Large EURO-CORDEX Regional Climate Model Ensemble. *Journal of Geophysical Research: Atmospheres*. Vol. 126, no. 17.

WORLD METEOROLOGICAL ORGANIZATION, 2024. *Climate*.

Acknowledgements

I want to express my gratitude towards my first supervisor Prof. G. G. Paulus, who directly sent me to Dr. Kleidon's working group for biospheric theory and modelling when I asked him where I could possibly do "something with physics and environment".

I want to thank my secondary assessor, Dr. Axel Kleidon, who included me into his working group and made me discover earth system sciences and climate data analysis and was always open to looking at interesting plots and findings and always gave constructive feedback, no matter the supposed naivety of the question.

I want to thank my working group, who is simply the best working group, and since nobody ever said that about their working group before, I can be completely certain that I am right about it actually being the best. They created an incredibly appreciative working environment where mistakes and difficulties and countless questions were accepted as an integral part of the process and they were always receptive to unlimited puns on maximum power, making it hard to feel pressured in the thesis writing process at all.

I especially want to thank Sarosh and Tejasvi who always were of best academic and emotional assistance, accepted last-minute proofreading sessions and initiated last-few-weeks table tennis sessions (after working hours of course). I leave this working group with a laughing (new exciting realms ahead) and a crying (old realms being a working group environment that I grew very fond of and will miss dearly) eye.

I also want to thank my friends and family who always supported my countless digressions from my initial physics studies and always helped me get back on the physics track. Specifically, Justus who kept me well-supplied with puns and pasta throughout this episode and Jette who took great care of my LaTeX indices.

I acknowledge the EURO-CORDEX consortium for providing the climate simulation data used in this work. I also thank the individual modeling groups and the European Centre for Medium-Range Weather Forecasts (ECMWF) for making the data available. I thank the NASA-CERES team for making the satellite data openly available and the DWD team for making their HYRAS observational data available.

Declaration of Academic Integrity

Jena, August 22, 2024

Annegret Roessler